HHS Public Access

Author manuscript

Bone. Author manuscript; available in PMC 2024 June 01.

Published in final edited form as:

Bone. 2024 June ; 183: 117085. doi:10.1016/j.bone.2024.117085.

Skeletal abnormalities in mice with *Dnmt3a* missense mutations

Austin Bell-Hensley[a,1], **Diana C. Beard**[b,1], **Kathryn Feeney**[a], **Hongjun Zheng**[c], **Yunhao Jiang**[a], **Xiyun Zhang**[b], **Jin Liu**[c], **Harrison Gabel**[b,*], **Audrey McAlinden**[c,d,e,**]

[a]Department of Biomedical Engineering, Washington University in St. Louis, St. Louis, MO, USA

[b]Department of Neuroscience, Washington University School of Medicine, St. Louis, MO, USA

[c]Department of Orthopaedic Surgery, Washington University in St. Louis, St. Louis, MO, USA

[d]Department of Cell Biology & Physiology, Washington University in St. Louis, St. Louis, MO, USA

[e]Shriners Hospital for Children – St. Louis, St. Louis, MO, USA

Abstract

Overgrowth and intellectual disability disorders in humans are typified by length/height and/or head circumference ≥ 2 standard deviations above the mean as well as intellectual disability and behavioral comorbidities, including autism and anxiety. Tatton-Brown-Rahman Syndrome is one type of overgrowth and intellectual disability disorder caused by heterozygous missense mutations in the DNA methyltransferase 3A (*DNMT3A*) gene. Numerous *DNMT3A* mutations have been identified in Tatton-Brown-Rahman Syndrome patients and may be associated with varying phenotype severities of clinical presentation. Two such mutations are the R882H and P904L mutations which result in severe and mild phenotypes, respectively. Mice with paralogous mutations (*Dnmt3a*$^{P900L/+}$ and *Dnmt3a*$^{R878H/+}$) exhibit overgrowth in their long bones (e.g., femur, humerus), but the mechanisms responsible for their skeletal overgrowth remain unknown. The goal of this study is to characterize skeletal phenotypes in mouse models of Tatton-Brown-Rahman Syndrome and identify potential cellular mechanisms involved in the skeletal overgrowth phenotype. We report that mature mice with the *Dnmt3a*$^{P900L/+}$ or *Dnmt3a*$^{R878H/+}$ mutation exhibit tibial overgrowth, cortical bone thinning, and weakened bone mechanical properties. *Dnmt3a*$^{R878H/+}$ mutants also contain larger bone marrow adipocytes while *Dnmt3a*$^{P900L/+}$ mutants show no adipocyte phenotype compared to control animals. To understand the potential cellular mechanisms regulating these phenotypes, growth plate chondrocytes, osteoblasts, and osteoclasts

*Corresponding author. gabelh@wustl.edu (H. Gabel). **Correspondence to: A. McAlinden, Department of Orthopaedic Surgery, Washington University in St. Louis, St. Louis, MO, USA. mcalindena@wustl.edu (A. McAlinden).
[1]Denotes co-first authors.

CRediT authorship contribution statement

Austin Bell-Hensley: Writing – review & editing, Writing – original draft, Visualization, Validation, Supervision, Project administration, Methodology, Investigation, Funding acquisition, Formal analysis, Data curation, Conceptualization. **Diana C. Beard:** Writing – review & editing, Methodology, Investigation, Funding acquisition, Formal analysis, Data curation, Conceptualization. **Kathryn Feeney:** Methodology, Investigation, Data curation. **Hongjun Zheng:** Methodology, Investigation. **Yunhao Jiang:** Methodology, Investigation. **Xiyun Zhang:** Methodology, Investigation. Jin Liu: Methodology, Investigation. **Harrison Gabel:** Writing – review & editing, Supervision, Resources, Project administration, Methodology, Funding acquisition, Formal analysis, Conceptualization. **Audrey McAlinden:** Writing – review & editing, Supervision, Resources, Project administration, Investigation, Funding acquisition, Formal analysis, Conceptualization.

Declaration of competing interest

All authors declare that they have no conflicts of interest.

were assessed in juvenile mutant mice using quantitative static histomorphometry and dynamic histomorphometry. Tibial growth plates appeared thicker in mutant juvenile mice, but no changes were observed in osteoblast activity or osteoclast number in the femoral mid-diaphysis. These studies reveal new skeletal phenotypes associated with Tatton-Brown-Rahman Syndrome in mice and provide a rationale to extend clinical assessments of patients with this condition to include bone density and quality testing. These findings may be also informative for skeletal characterization of other mouse models presenting with overgrowth and intellectual disability phenotypes.

Keywords

Overgrowth and intellectual disability; OGID; Tatton-Brown-Rahman Syndrome; TBRS; DNMT3A overgrowth syndrome; DOS; DNMT3A; Skeletal overgrowth; Skeletal development; Mouse model

1. Introduction

Overgrowth and intellectual disability (OGID) disorders are typified by length/height and/or head circumference ≥ 2 standard deviations above the mean in addition to other abnormalities, most commonly intellectual disability [1,2]. Several neurodevelopmental disorders – including Tatton-Brown-Rahman, Sotos, Malan, Weaver, Homo-cystinuria, 22q13 deletion, and Bannayan-Riley-Ruvalcaba syndromes – meet the criteria for OGID [3]. While OGID disorders share a few hallmark phenotypes, there is a high degree of heterogeneity associated with OGID patients that is poorly understood.

As multi-omic approaches become more accessible clinically, exome and genome sequencing data have been collected from OGID patients to identify associated genetic variants. DNA sequencing on a population of 710 individuals with OGID identified that ~44 % of OGID disorders are caused by mutations in 6 epigenetic genes: *NSD1*, *EZH2*, *EED*, *CHD8*, *HIST1H1E*, and *DNMT3A* [4]. Epigenetic mechanisms affected by these causal mutations include regulation transcription by modifying DNA methylation (*DNMT3A*), the methylation of histones (*NSD1*, *EZH2*, *EED*), and chromatin structure (*CHD8*, *HIST1H1E*) [4]. Each of these epigenetic regulators is involved in modulating the expression of numerous genes, making it difficult to identify a therapeutic approach that targets specific dysregulated genes. Further complicating mechanistic studies, diverse causal mutations have been identified in each of these genes including nonsense, missense, and frameshift mutations [4]. These complications necessitate comparing multiple mutations within each gene to better understand the molecular underpinnings associated with OGID phenotypes.

One of the most commonly mutated genes in patients with OGID caused by disruption of epigenetic regulators is DNA methyltransferase 3A (*DNMT3A*) [4], a de novo methyl transferase that is critical for embryonic and postnatal development [5]. Patients with mutations in *DNMT3A* who exhibit OGID symptoms are diagnosed with Tatton-Brown-Rahman Syndrome (TBRS), also known as *DNMT3A* Overgrowth Syndrome (DOS) [6]. The first publications that identified [7] and confirmed [8] *DNMT3A* as a gene of interest for OGID found a number of different mutations in regions encoding the functional

domains of DNMT3A. Methylomic analysis of peripheral blood cells from patients with TBRS found that different variants in *DNMT3A* result in differential disruption of DNA methylation. Missense mutations at the Arg882 (R882) position result in severe genome-wide demethylation while other *DNMT3A* mutations, including missense mutations and a 135 kb gene deletion, cause a more moderate reduction of methylation [9]. However, the severity of neurodevelopmental and skeletal abnormalities did not correlate strongly with mutation or methylomic profile, a phenomenon that is not well understood. In vitro models have demonstrated that the disease-associated R882H and P904L mutations cause reductions in DNA methylation [10], and mouse models engineered to express *Dnmt3a* mutations (*Dnmt3a*$^{R878H/+}$ and *Dnmt3a*$^{P900L/+}$; homologous to the human *DNMT3A*$^{R882H/+}$ and *DNMT3A*$^{P904L/+}$mutations, respectively) have been generated to better understand the molecular mechanisms that cause TBRS. These mutant animals recapitulate many aspects of the human disorder, such as obesity, long bone overgrowth, and behavioral alterations [9,11]. While transcriptomics and methylomics have been used to characterize neuronal and hematopoietic phenotypes of these mouse models, the molecular underpinnings of skeletal overgrowth remain poorly understood.

Mechanisms of overgrowth are understudied in mouse models of OGID, despite being highlighted as a hallmark phenotype in humans with these disorders. Early researchers predicted that overgrowth may result from increased proliferation, hypertrophy, or extracellular matrix production in growth plate chondrocytes [12]. More recent work has advanced the clinical understanding of genotype-phenotype correlations in OGID disorders, suggesting that the overgrowth may be caused by disruption of the PI3K/mTOR signaling pathway which can inhibit apoptosis and promote cell growth and proliferation [13,14]. However, the limited availability of well-characterized mouse models has made studying these mechanisms difficult. Given the overlap of skeletal phenotypes among OGID disorders, skeletal characterization of mouse models will play an important role in understanding biological mechanisms responsible for skeletal abnormalities associated with these diseases. Thus, studies of TBRS mouse models can provide a basis for studying skeletal overgrowth in mouse models of OGID.

In this study, the *Dnmt3a*$^{R878H/+}$ and *Dnmt3a*$^{P900L/+}$ mouse models of TBRS were examined for skeletal abnormalities in mature and developing mice. Previous work has reported overgrowth in long bones (e.g., femur, humerus), but studies to decipher the mechanisms driving these skeletal phenotypes are limited. Here, we report that mature mice harboring *Dnmt3a*$^{R878H/+}$ and *Dnmt3a*$^{P900L/+}$ mutations have tibia overgrowth, thinner femoral and tibial cortical bone, and weakened femoral mechanical properties. We also report a mutation-specific increase in tibial bone marrow adipocyte size. To determine the developmental origins of these phenotypes, growth plate chondrocytes, osteoblasts, and osteoclasts were assessed in skeletally developing juvenile mice. While osteoblast activity and osteoclast number are similar between wild-type and mutant littermate pairs, growth plate thickness is increased in juvenile mutant mice with either mutation. Through analysis of mouse models of *Dnmt3a* mutations, the role of this DNA methyltransferase in bone development and growth can be better understood, and this can be used as a case study for understanding skeletal phenotypes in other OGID disorders.

2. Material and methods

2.1. Animal husbandry

Mice were housed in a room on a 12:12 h light/dark cycle, with controlled room temperature (20–22 °C) and relative humidity (50 %). Individually ventilated home cages (36.2 × 17.1 × 13 cm) were supplied with corncob bedding and free access to water and standard laboratory chow (PicoLab Irradiated Rodent Diet 5053). Adequate measures were taken to minimize animal pain or discomfort, and all mice were group-housed in mixed-genotype, single-sex cages. All animal protocols were approved by the Institutional Animal Care and Use Committee and the Animal Studies Committee of Washington University in St. Louis, and in accordance with guidelines from the National Institutes of Health (NIH).

2.2. Transgenic animals

Dnmt3a$^{R878H/+}$ and *Dnmt3a*$^{P900L/+}$ animals were generated as previously described [9,11]. Both mutant strains were backcrossed to C57BL6/J females (JAX Stock No. 000664) and propagated separately. Mutant males and WT females were used for the generation of experimental animals to avoid any differences in mothering from mutant dams. Mice were genotyped with ear DNA by PCR for either *Dnmt3a*$^{R878H/+}$ and *Dnmt3a*$^{P900L/+}$ mutations as previously described [9,11].

2.3. EchoMRI

Body composition was measured with whole-body quantitative magnetic resonance using an EchoMRI Body Composition Analyzer at the Washington University Diabetes Research Center, and experiments were performed as previously described [15]. In brief, live animals were placed in a plastic cylinder tube with a solid insert to limit movement, and the signal in response to a low-intensity electromagnetic field was used to measure the relaxation of spin curves, allowing for the quantification of fat and lean tissue volume. To standardize between recording days, measurements were calibrated to Canola oil prior to each recording session.

2.4. Tissue collection

Animals were weighed prior to euthanasia, and hindlimbs was harvested from juvenile animals at postnatal day 27 (P27), and from mature animals at 30- to 36-weeks of age. Whole right hindlimbs from juvenile and mature mice were fixed and decalcified for paraffin-embedded histology. Left hindlimbs dissected from mature mice and left tibias from juvenile mice were wrapped in PBS-wetted gauze and frozen at −20 °C for bone length assessment. Left femurs from juvenile mice were stored in 70 % ethanol at 4 °C until they were embedded in methyl methacrylate (MMA) for histology.

2.5. Bone length assessment

Bone length was measured in left tibias from mature mice. Before imaging, left hindlimbs from mature mice were thawed at room temperature for 2 h and tibias were isolated by scalpel dissection. X-ray radiographs were taken with 6s exposures at 45kV (Faxitron Ultrafocus 100; Faxitron Bioptics, LLC, Tucson, AZ, USA) and the tibias were measured using the “Measure” tool on Faxitron Vision Software (Version 2.3.1). As a secondary

measure, tibia lengths were also measured using a Vernier caliper which yielded similar results (data not shown). After X-ray radiography, tibias and femurs were wrapped in PBS-wetted gauze and frozen at −20 °C for subsequent micro-computed tomography analysis.

2.6. Micro-computed tomography

Whole bone 3D micro-computed tomography (μCT) was performed on left femurs and tibias from mature mice using standard methods [16]. Before imaging, left hindlimbs from mature mice previously dissected for bone length assessments were thawed at room temperature for 2 h. Up to 5 femurs or 5 tibias were embedded in 2 % agarose gel (w/v in distilled water) and scanned in a cabinet μCT scanner (Scanco μCT50; SCANCO Medical AG, Brüttisellen, Switzerland) and the images were analyzed with Scanco Eval Program with a lower threshold of 350. Analyzed regions for the femur include the mid-diaphysis (midpoint of bone +/− 50 slices) for cortical bone outcomes and the distal metaphysis (150 slices leading up to the most proximal slice of the distal growth plate) for trabecular bone outcomes. For the tibia, the whole bones were analyzed for total volume, bone volume, and marrow volume for the normalization of osmium analyses and for cortical bone indices at the mid-diaphysis (midpoint of bone +/− 50 slices). After μCT radiography, tibias and femurs were wrapped in PBS-wetted gauze and frozen at −20 °C for subsequent biomechanical analysis or osmium staining.

2.7. Biomechanical analysis

Three-point bend testing was performed on left femurs from mature mice after scans were taken for bone length and μCT analyses, following published guidelines [17]. Before testing, the femurs were thawed at room temperature for 2 h. Excess tissues were removed from the femurs using forceps and gauze. Femur length was measured with a Vernier caliper and the midpoint of the bone was marked with a pencil. A material testing machine (ElectroPuls E1000; Instron, Norwood, MA, USA) was set up with a 7 mm span and femurs were placed into the load frame with the femoral condyles facing up and the proximal end of the bone positioned on the left side. Femurs were manually positioned and loaded to approximately −0.3 N before switching to the machine's load control. A pre-load of −0.5 N was applied for 5 s then a sine wave function (1 Hz frequency, 3.75 N amplitude, 5 cycles, 90° starting phase) was used to help pre-condition the bone. Immediately after pre-conditioning the bone, the machine applied a ramp to failure test with a ramp rate of 0.1 mm/s. Each femur was observed during testing to ensure the bone did not shift or experience other phenomena that could affect mechanical readouts. Bones were loaded until complete fracture then the loading program was manually stopped, and the test data was saved. Force-displacement data were analyzed to determine structural mechanical properties (e.g., maximum load) and were also used to estimate material properties (e.g., maximum stress) as described [17].

2.8. Osmium staining and analysis

Osmium staining was performed on left tibias from mature mice as described in previous publications [18,19]. Prior to fixation, left hindlimbs from mature mice previously dissected for bone length and μCT assessments were thawed at room temperature for 2 h. Excess tissues were removed from the tibias using forceps and gauze. Bones were then fixed in 10 % NBF for 24 h at room temperature. Fixed bones were rinsed in distilled water and

then decalcified using 14 % EDTA (pH 7.4) for 14 days, refreshing the EDTA every 3–4 days. Decalcified bones were rinsed in distilled water and then stored in DPBS at 4 °C until osmium staining (<2 weeks). Decalcified bones were stained in 1 mL of a 1 % osmium tetroxide (Electron Microscopy Services, Hatfield, PA, USA), 2.5 % potassium dichromate (Sigma-Aldrich, St. Louis, MO, USA) solution in 1× PBS for 48 h at room temperature, then rinsed with distilled water. Osmium-stained samples were stored in 1× PBS at 4 °C until μCT scanning (<2 weeks). Up to 11 tibias were embedded in 2 % agarose gel (*w/v* in distilled water) and scanned with 10 μm voxel resolution using a Scanco μCT50 (SCANCO Medical AG, Brüttisellen, Switzerland), and the radiographs were analyzed with Scanco Eval Program. The entire lengths of the tibias were scanned and the proximal metaphysis (200 slices distal to the proximal growth plate) of each tibia was contoured and analyzed with a lower threshold of 400. This threshold detects osmium-stained bone marrow adipose tissue without detecting any of the demineralized bone. Contours and analyses were completed by one blinded assessor. After μCT scanning, the bones were stored in 1× PBS at 4 °C for future analysis.

2.9. Histology

Right hindlimbs from mature and juvenile mice were dissected by cutting through the hip joint with a scalpel and dislocating the femoral head out of the joint. The hindlimbs were fixed in 10 % neutral bufferedformalin for 24–48 h at room temperature. After fixation, the juvenile samples were briefly rinsed in PBS then decalcified in 14 % EDTA for 14 days, refreshing the EDTA every 3–4 days, while the mature hindlimbs were decalcified in formic acid (ImmunoCal™ Decalcifier; StatLab, McKinney, TX, USA) for 3–4 days, refreshing the EDTA every 1–2 days. The decalcified hindlimbs were rinsed in distilled water then stored in DPBS at 4 °C for up to 3 weeks or until they could be embedded in paraffin blocks. Paraffin-embedded tissues were sectioned in the sagittal plane to generate 10 μm thick tissue slices which were then mounted onto glass microscopy slides. Mounted tissues from mature mice were stained using a standard hematoxylin and eosin (H&E) staining technique. Mounted tissues from juvenile mice were stained with toluidine blue or designated for immunohistochemistry (IHC). IHC staining was completed for proliferating cell nuclear antigen (PCNA) using a monoclonal antibody (#13110; Cell Signaling, Danvers, MA, USA) and a polyclonal goat anti-rabbit HRP secondary antibody (#P044801–2; Agilent, Santa Clara, CA, USA). After all types of staining, samples were covered with a mounting medium (Cytoseal™ XYL; Richard-Allan Scientific, Kalamazoo, MI, USA) and a glass coverslip. Brightfield imaging of stained slides was completed on a whole slide imaging system (Hamamatsu Photonics Nanozoomer 2.0-HT System; Hamamatsu City, Shizuoka, Japan) using a 20× magnification lens.

2.10. Bone marrow adipose tissue quantification

Images of the H&E-stained proximal tibia metaphysis from the right hindlimb were exported at 10× magnification. The images were imported into ImageJ software for analysis. Using a scale of 1.084 pixels/μm (verified by measuring scale bar), the bone marrow adipocyte average cross-sectional area was quantified. Briefly, the bone marrow cavity was selected using ImageJ tools (e.g., threshold, median filter, fill holes, wand) and then the cross-sectional area of the marrow cavity was measured. Within the bone marrow cavity, the

ImageJ tool “Particle Analyzer” was used to select adipocyte-like shapes in the image by filtering for particles sized 100 to “infinity” μm and circularity 0.0 to 1.0. Non-adipocytes were manually removed using ImageJ tools (e.g., median filter, fill holes, wand, clear, fill, watershed). This manual selection step was repeated by three independent, blinded assessors. Remaining adipocytes were analyzed with the “Particle Analyzer” by filtering for particles sized 100 to 4000 μm and circularity 0.5 to 1.0. The total number of adipocytes and the area of each individual adipocyte were recorded, then the average adipocyte area was calculated. Values recorded by each of the three assessors were averaged to give an accurate representation.

2.11. Growth plate analysis

Images of the toluidine blue-stained proximal tibia and distal femoral growth plates from juvenile right hindlimbs were exported at 5× magnification. The images were imported into ImageJ software for analysis. Using a scale of 0.542 pixels/μm (verified by measuring scale bar), the thickness of the whole growth plate and each zone within the growth plate (resting, proliferating, and hypertrophic) were quantified. Since the growth plate thickness is not uniform across the entire growth plate, ten measurements were taken, evenly spaced across the width of the growth plate, for the full growth plate thickness as well as each zone within the growth plate. The average of the ten measurements was used as a representative thickness of the growth plate or growth plate zone. The sum of the thicknesses for the three zones (resting, proliferating, and hypertrophic) of each growth plate was compared to the total growth plate thickness and was required to have ≤5 % difference. For zones that added up to >5 % difference from the total growth plate thickness, all three zones were re-measured. Measurements were taken by one blinded assessor.

2.12. Proliferating cell nuclear antigen analysis

Images of the PCNA-IHC stained proximal tibia and distal femoral growth plate tissue sections from juvenile right hindlimbs were exported at 5× magnification. The images were imported into ImageJ software for analysis. Using a scale of 0.542 pixels/μm (verified by measuring scale bar), the $PCNA^+$ cell density and average cross-sectional area were quantified. Briefly, the growth plate was selected using the ImageJ “Polygon Selection” tool and then the cross-sectional area of the growth plate was measured. Within the growth plate, $PCNA^-$ cells were removed using ImageJ tools (e.g., threshold, median filter, fill holes, wand, clear, fill, watershed). Remaining $PCNA^+$ cells were analyzed with the “Particle Analyzer” by filtering for particles size 0 to 500 μm and circularity 0.0 to 1.0. The total number of $PCNA^+$ cells and the area of each individual $PCNA^+$ cell were recorded, then the average $PCNA^+$ cell area and $PCNA^+$ cell density were calculated. Measurements were taken by one blinded assessor.

2.13. Dynamic histomorphometry

Dynamic histomorphometry was performed on left femurs from juvenile mice following established protocols [20,21]. Briefly, the mice were given intraperitoneal injections of calcein (10mg/kg; Sigma–Aldrich, St. Louis, MO, USA) at 21 days of age and alizarin (30mg/kg; Sigma–Aldrich, St. Louis, MO, USA) at 25 days of age to label the endosteal and periosteal surfaces. Bones were stored in 70 % ethanol at 4 °C until MMA embedding.

These femurs were embedded in MMA as previously described [22], and measured using a Vernier caliper to locate the mid-diaphysis. Three transverse sections were cut from the mid-diaphysis region using a saw microtome (SP1600 Saw Microtome; Leica, Wetzler, Germany) and mounted onto glass microscopy slides using a mounting medium (Cytoseal™ XYL; Richard-Allan Scientific, Kalamazoo, MI, USA) and a glass coverslip. Sections were imaged using a confocal microscope (DMi8; Leica, Wetzler, Germany) with the following settings: 10× lens, 2048 × 2048 resolution, 400 Hz scan speed, 20 μm z-stack size, and 5 z-stack images. Images were analyzed using BIOQUANT OSTEO (BIOQUANT Image Analysis, Nashville, TN, USA). Analysis was completed by one blinded assessor.

2.14. Osteoclast assessment

Images of the TRAP-stained femur mid-diaphysis from each juvenile left femur were exported at 10× magnification. The images were imported into ImageJ software for analysis. Using a scale of 1.084 pixels/μm (verified by measuring scale bar), periosteal bone surface, number of osteoclasts, and bone surface area of each osteoclast were quantified. Briefly, the endocortical surface of the bone was outlined using the ImageJ “Polygon Selection” tool and then the perimeter of the endocortical surface was measured. Along the endocortical surface, the bone surface area of each osteoclast was traced using the ImageJ “Freehand Line” tool and the length of the line was measured. The total number of osteoclasts and the bone surface are of each osteoclast was recorded, then the osteoclast number per bone surface and osteoclast surface per bone surface were calculated. Measurements were taken by one blinded assessor.

2.15. Statistical analysis

Data were analyzed and plotted using GraphPad Prism 9.4.0. All analyses were performed using two-way ANOVAs using sex and genotype as sources of variation. Multiple comparisons were made between equal numbers of sex-matched, littermate-paired animals after correcting for multiple comparisons using the Šídák method unless otherwise noted. While *Dnmt3a* mutations are not known to cause prominent sexually dimorphic phenotypes in mice [11], significance testing was performed using two-way ANOVA to test for sexually-dimorphic and genotype effects, given the known sexual dimorphism in C57BL/6J skeletal development [23]. Full ANOVA results can be found in Supplementary Table 1. Unless specified, descriptive statistics for each graph indicate median with individual values represented as solid circles or square frames. Significance is indicated for comparisons that meet the threshold $p \leq 0.05$ unless otherwise indicated.

3. Results

3.1. Dnmt3a point mutations result in tibia length increase in mature mice

The first publications characterizing heterozygous *Dnmt3a*$^{R878H/+}$ and *Dnmt3a*$^{P900L/+}$ mouse models of TBRS report significantly longer femurs in male and female mutant mice compared to wild-type (WT) littermates at 30- to 36-weeks old [9,11]. To fully assess the impact of *Dnmt3a* mutations in long bones of the leg, we performed analysis of tibia length in mature 30- to 36-week-old male and female *Dnmt3a*$^{R878H/+}$ and *Dnmt3a*$^{P900L/+}$ mice by digital X-ray (Fig. 1A, B) and physically via Vernier caliper (data not shown). We observe

a small significant increase in tibial length in R878H mutants, and a trending increase in *Dnmt3a*$^{P900L/+}$ mutants, with a significant tibia length increase in *Dnmt3a*$^{P900L/+}$ females. Considering that bones are mechanoresponsive [17], this pattern has been compared to body weight trends in the same mice (Fig. 1C). However, under the normal chow feeding conditions of this study, only the *Dnmt3a*$^{R878H/+}$ mutant mice show an increase in body weight compared to WT littermates, suggesting that the trend towards tibial overgrowth in *Dnmt3a*$^{P900L/+}$ mutants is not a result of increased mechanical loading. In summary, mice with either the *Dnmt3a*$^{P900L/+}$ or *Dnmt3a*$^{R878H/+}$ mutation have tibial overgrowth and only the *Dnmt3a*$^{R878H/+}$ mice exhibit increased body weight.

3.2. Cortical bone thinning in mature mice with Dnmt3a mutations

To investigate if additional skeletal abnormalities occur in *Dnmt3a*$^{P900L/+}$ and *Dnmt3a*$^{R878H/+}$ mutant mice [9,11], micro-computed tomography (μCT) analysis was carried out on 30- to 36-week-old mice. While no significant differences in femoral trabecular bone volume per tissue volume (BV/TV) are seen between WT and mutant mice (Supp. Fig. 1A–G), femoral mid-diaphysis cortical bone thickness is significantly reduced in mice with either the *Dnmt3a*$^{P900L/+}$ or the *Dnmt3a*$^{R878H/+}$ heterozygous mutation (Fig. 2A–B). Cortical tissue mineral density, marrow volume, and total volume are unchanged with either mutation (Fig. 2C–E). While there are sex differences in this data, these differences are expected given the known sexual dimorphism in the skeletal development of C57BL/6J mice [23]. As such, post-hoc comparisons have not been made between male and female groups. Similar trends in mid-diaphysis cortical bone thickness and tissue mineral density are also observed in tibias from both the *Dnmt3a*$^{P900L/+}$ and the *Dnmt3a*$^{R878H/+}$ mutant mice (Fig. 3A–C). However, there is a reduction in tibia marrow volume and total volume found only in the *Dnmt3a*$^{R878H/+}$ female mice (Fig. 3D–E). In summary, mice with either the *Dnmt3a*$^{P900L/+}$ or *Dnmt3a*$^{R878H/+}$ mutation have thinner cortical bone in the mid-diaphysis of their femurs and tibias, and female mice with the *Dnmt3a*$^{R878H/+}$ mutation have reduced total volume and marrow volume.

3.3. Mature mice with Dnmt3a mutations have altered bone biomechanics

To assess if the thinner cortical bone phenotype translates to altered bone mechanical properties, ex vivo three-point bend testing was carried out on femurs from 30- to 36-week-old mice. The mechanical testing data shows that the bones of the mutant mice have significantly lower stiffness, yield load, and maximum load than the femurs of WT littermates (Fig. 4A–E). ANOVA on the *Dnmt3a*$^{P900L/+}$ yield load data indicates a significant sex-genotype interaction effect indicating that the *Dnmt3a*$^{P900L/+}$ mutation has a larger effect size in females than it does in males. Of note, the post-yield displacement and work-to-fracture for these mice remain the same (Fig. 4F–G) suggesting that the brittleness of the bones is unchanged. Biomechanical properties have been normalized to the femoral mid-diaphysis cross-sectional area (measured using μCT) to estimate material properties. When normalized, mutant mice have reduced Young's modulus, yield stress, and ultimate stress (Supp. Fig. 2A–C). In summary, the femurs of mutant mice are less stiff and are weaker than those of WT mice, consistent with their reduced cortical bone thickness.

3.4. Bone marrow adipose tissue increases in mature Dnmt3a$^{R878H/+}$ mice

Given the decreased cortical thickness and known role for *DNMT3A* mutations in acute myeloid leukemia (AML) [24], cells in the marrow cavity are also of interest. Osmium tetroxide staining of bone marrow adipose tissue (BMAT) shows that a group (2 out of 9; 22 %) of *Dnmt3a*$^{R878H/+}$ mutant female mice displayed a robust (>1 mm^3) increase in adipocyte volume in the tibia proximal metaphysis. However, this increase is not present in all R878H mutant females and is not found in the males (Fig. 5A–B). There is a trend towards an increase in BMAT volume in the *Dnmt3a*$^{P900L/+}$ mutants, but the effect size is more modest than the upregulation seen in the *Dnmt3a*$^{R878H/+}$ mutants. Hematoxylin and Eosin (H&E) staining in the tibia proximal metaphysis shows that the cross-sectional area of bone marrow adipocytes is increased in the *Dnmt3a*$^{R878H/+}$ mutant mice, but not in the *Dnmt3a*$^{P900L/+}$ mutant mice (Fig. 5C–D). In summary, bone marrow adipocyte cross-sectional area and bone marrow adipose tissue volume are increased in the proximal tibia metaphysis in *Dnmt3a*$^{R878H/+}$ mutants, but not in *Dnmt3a*$^{P900L/+}$ mutants.

3.5. Growth plate thickening occurs in the hindlimbs of juvenile mice with Dnmt3a mutations

To identify developmental mechanisms involved in the skeletal overgrowth and cortical bone thinning found in the mature mutant mice, juvenile mice were assessed. Male and female C57BL/6J mice begin a period of rapid growth around 4 weeks of age, suggesting that this would be an appropriate time point for growth plate analysis [25,26]. To better understand the mechanisms responsible for the observed femoral and tibial overgrowth trends in the mature mice, the thickness and proliferative activity in the growth plates of juvenile mutant mice were quantified as these are highly correlated with bone length and bone growth rate [27]. Growth plates in the proximal tibias of mutant juvenile mice are slightly thicker in mice with either the *Dnmt3a*$^{R878H/+}$ or *Dnmt3a*$^{P900L/+}$ mutation (Fig. 6A–B), suggesting that growth plate regulation is responsible for the tibial overgrowth observed in the mature mutant mice. This increase in thickness is not specific to the resting zone, proliferating zone, or hypertrophic zone of the growth plate, as each zone maintains a consistent proportion of the total growth plate thickness (Fig. 6C). Immunohistochemical staining of Proliferating Cell Nuclear Antigen (PCNA) indicates that there is no change in the density or cross-sectional area of PCNA$^+$ cells in mutant mice (Fig. 6D–F). There is also a slight trend towards growth plate thickening in the distal femur growth plate (Supp. Fig. 3A–B), though it is difficult to identify a consistent, representative thickness measurement in the irregularly shaped femoral growth plates. In the distal femur growth plates, males with either the *Dnmt3a*$^{P900L/+}$ or the *Dnmt3a*$^{R878H/+}$ mutation trend towards having larger PCNA$^+$ cells with higher density than their WT littermates. However, PCNA$^+$ cells in the distal femur growth plate of females with either mutation trend towards being smaller and had lower cell density than their controls (Supp. Fig. 3C–E). In summary, the proximal tibial growth plate is significantly thicker in juvenile mutant mice and may explain the overgrowth observed in the tibias of mature mice.

3.6. Assessment of bone formation and osteoclast number in juvenile Dnmt3a mutants

Mice were analyzed at 3 to 4 weeks of age to discern the cellular basis for cortical thinning. TRAP staining of transverse sections at the femur mid-diaphysis indicates that there is no significant change in osteoclast number or osteoclast surface per bone surface on the endocortical surface (Fig. 7A–C). On the other hand, dynamic histomorphometry on the femur mid-diaphysis in these juvenile mice indicates that there is no change in bone formation indices in mutant mice, suggesting that there is no difference in osteoblast activity between WT and mutant mice (Fig. 7D–F). Of note, the WT and mutant mice in the *Dnmt3a*$^{R878H/+}$ litters did not consistently take up the alizarin dye (red color in Fig. 7E–F) making it difficult to draw conclusions about these mice. Mice that did not take up the alizarin dye have their bone formation rate (BFR) for both the endocortical (Ec.) and periosteal (Ps.) surface set to 0.15 μm/day based on minimum values established by Foldes et al. [28]. Mineral apposition rate and mineralizing surface per bone surface values are also unchanged between WT and mutant animals (Supp. Fig. 4A–D). In summary, it is unclear if osteoblasts or osteoclasts are responsible for the cortical thinning phenotype observed in mature *Dnmt3a* mutant mice.

4. Discussion

The cellular and molecular mechanisms of skeletal overgrowth in OGIDs are poorly understood. Genetic mouse models show promise in recapitulating skeletal, behavioral, and hematopoietic changes observed in TBRS patients. This TBRS model can be used to study skeletal overgrowth associated with OGID and begin to identify the biological mechanisms responsible for their skeletal phenotypes. Previous *Dnmt3a* knockout studies have highlighted a critical role for this DNA methyltransferase enzyme in regulating musculoskeletal development [29]. Mice with homozygous *Dnmt3a* knockout are severely runted and have poor survival beyond 4 weeks of age while heterozygous *Dnmt3a* knockout mice survive to maturity, but develop obesity, extended long bones, and behavioral abnormalities [10,30]. Here, we use two genetic mouse models, *Dnmt3a*$^{P900L/+}$ and *Dnmt3a*$^{R878H/+}$, to identify skeletal phenotypes that have not yet been characterized in human patients with paralogous mutations. Further, we attempted to examine potential cellular mechanisms that may be driving skeletal overgrowth and other bone abnormalities in these TBRS mouse models.

There is tibial overgrowth in 30- to 36-week-old *Dnmt3a*$^{R878H/+}$and *Dnmt3a*$^{P900L/+}$ mutants, similar to the femur overgrowth that has been previously reported [9,11]. In both the femur [9,11] and tibia, a slightly larger effect size in female mutant mice suggests a potential sex-related effect of these mutations. Bone length is known to correlate with body mass suggesting that tibial overgrowth may be a result of increased body mass [17]. Earlier studies have reported that *Dnmt3a* mutant mice accumulate fat mass and overall body weight more quickly than WT littermates, particularly for female mice fed a high fat diet [10,11]. Meanwhile, it has been reported that male and female *Dnmt3a*$^{P900L/+}$ mice have a trend towards increase in overall body weight driven by an increase in fat mass [11]. However, the analysis of body weights for mice fed standard chow reported here showed no increase in *Dnmt3a*$^{P900L/+}$ mutants at 30 to 36 weeks of age, suggesting that the femoral and tibial

overgrowth may be a result of other biological phenomena. While the overgrowth effect size is larger in the femurs [11], future skeletal evaluations of these TBRS mouse models, and perhaps other OGID mouse models, can study overgrowth in either the femur or the tibia.

Analyses in 27-day-old, skeletally developing mice show that this overgrowth may be driven by dysregulation of growth plate thickness during skeletal maturation. Mice with either the *Dnmt3a*$^{P900L/+}$ or *Dnmt3a*$^{R878H/+}$ mutation show growth plate thickening in the proximal tibia. However, PCNA staining suggests that there is no change in proliferating cell density or cell size with either mutation in the proximal tibia growth plate. However, this is only indicative that there is no change in PCNA positive cells at one specific time point as analyzed in this study (P27). Others have shown differences in tibial growth plate PCNA staining at post-natal day 7 [31] and 14 [32] and tibial epiphysis chondrocyte PCNA staining at embryonic days 16.5 and 18.5 [33] in C57Bl/6 mice. Therefore, it is possible that with analysis of other time points pre- or post-development, significant differences in PCNA positive cells may be found. Given that increases in body weight can affect numerous skeletal phenotypes [17], and progressive obesity phenotypes have been reported in *Dnmt3a* mutants [9–11], we measured body weight and carried out EchoMRI body composition analyses in the juvenile mice to ensure that they were not obese. The *Dnmt3a*$^{R878H/+}$ mutants had small reductions in body weights and decreased lean mass, while the *Dnmt3a*$^{P900L/+}$ mutant mice had no change in overall weight, lean mass, or fat mass (Supp. Fig. 5A–E). This shows that mutants do not demonstrate obesity phenotypes at this developmental timepoint, and growth plate analyses should be indicative of genotype effects. Future studies to analyze in vivo BrdU incorporation as well as static histomorphometry at earlier developmental time points may shed additional light on the involvement of proliferating growth plate cells in the overgrowth of tibias and femurs. It may also be interesting, in future studies, to examine extracellular matrix (ECM) accumulation in the growth plate as another potential explanation for the observed increases in growth plate thickness. Due to the irregular shape of the distal femoral growth plate, future animal studies of TBRS and other OGID syndromes that focus on the proximal tibial growth plate may be most fruitful.

The most robust phenotype observed across both sexes and both point mutations was cortical thinning in the femur and tibia mid-diaphysis of 30- to 36-week-old mice. This phenotype has not previously been reported in TBRS patients and has important implications, including possible reduced bone strength. Importantly, μCT analysis also shows that tissue mineral density is unchanged between WT and mutant animals from both sexes with either mutation indicating that hydroxyapatite is being deposited similarly in WT and mutant animals. However, three-point bend testing showed reduced strength, yield load, and maximum load for femurs in mice with either the *Dnmt3a*$^{P900L/+}$ or the *Dnmt3a*$^{R878H/+}$ mutation. Reduced bone strength is commonly associated with increased fracture risk which has not been widely reported in TBRS patients or the broader OGID patient community. Numerous comorbidities in individuals with TBRS or other OGID disorders have been reported, including musculoskeletal issues like joint hypermobility and kyphoscoliosis, and these complex phenotypes may have thus far obscured the recognition of increased fracture susceptibility in these patient populations due to weaker bones [8]. It would be worthwhile

to assess cortical bone thickness and strength in these patient populations to inform clinical decision-making and improve patient quality of life.

We investigated bone formation and osteoclast number in juvenile mutant mice at 27 days of age to determine what cells may be responsible for creating thinner cortical bone. Mice with osteoclast specific *Dnmt3a* knockout experience impaired osteoclastogenesis and exhibit a dramatic increase in trabecular bone volume per tissue volume [34], a phenotype that was not seen in this study. This suggests that heterozygous mutation in $Dnmt3a^{R878H/+}$ and $Dnmt3a^{P900L/+}$ mice has a qualitatively different impact on osteoclast biology than complete loss of function. In vitro studies in human cells found that *DNMT3A* upregulation increased methylation on promotors for *RUNX2*, *OSX*, and *IRF8*, promoting osteoclast differentiation and inhibiting osteoblast differentiation [35], suggesting that partial loss of *Dnmt3a* may increase cortical thickness. Given that our results conflict with these previous studies on *Dnmt3a* knockout mice and *Dnmt3a* overexpression in vitro, we believe that studying heterozygous mutations of *Dnmt3a* that precisely mimic the molecular etiology of TBRS is essential for understanding the potential impact on cortical thickness and bone length in OGID.

Since tissue mineral density of the bone was unchanged in the $Dnmt3a^{R878H/+}$ and $Dnmt3a^{P900L/+}$, we hypothesized that osteoclasts may be responsible for the changes in cortical thickness. Dynamic histomorphometry showed no significant differences in bone formation rate between the WT and mutant groups for either sex, suggesting that osteoblast activity may not be impacted. However, quantification of TRAP staining showed that there were also no apparent changes in osteoclast number or osteoclast surface area in mice with either the $Dnmt3a^{P900L/+}$ or the $Dnmt3a^{R878H/+}$ mutation. Future studies involving in vitro osteoblast and osteoclast functional assays in cells with these *Dnmt3a* mutations may be informative. Given the crosstalk and regulatory feedback that occurs in vivo between skeletal cells (osteoblasts, osteocytes, osteoclasts, marrow resident skeletal progenitor cells), it may be difficult to decipher cellular mechanisms in vitro via analyses of one cell type in isolation. In addition, Cre-inducible $Dnmt3a^{fl\text{-}R878H}$ mice (JAX Stock No. 032289) may serve as a key tool for delineating the effects of *Dnmt3a* mutations on osteoblast (Osterix-Cre), osteoclast (Cathepsin K-Cre), and growth plate chondrocyte (Aggrecan-Cre) development. Bulk and single-cell transcriptomics and methylomics of bone and bone marrow cells will also be critical for identifying the gene networks and molecular mechanisms disrupted in skeletal tissues of *Dnmt3a* mutants.

Although no differences in tissue mineral density were observed, cortical bone thinning in the *Dnmt3a* mutant animals is a reasonable explanation for the reduction in bone mechanical properties identified in this study (i.e. stiffness, maximum load, and load-to-fracture). However, one cannot rule out the possibility that the material composition of bones in the mutant animals may also be altered and contribute to the mechanical property defects [36,37]. Common approaches for characterizing bone quality include Raman spectroscopy to measure mineral-to-matrix ratios and mineral maturity/crystallinity [38], nanoindentation to detect changes at the microscale level [39], and quantitative backscattered scanning electron imaging (qBEI) to assess calcium concentration and distribution [40]. Changes in the bone collagen extracellular matrix (collagen fiber size, alignment, cross-linking) may

also contribute to altered mechanical properties [41–43]. These are all avenues for future studies to thoroughly characterize the bones of *Dnmt3a* mutant mice to further understand why the bones are mechanically compromised.

In the emerging field of musculoskeletal crosstalk, it has become clear that fat cells can communicate with bone and cartilage cells [44–46]. As such, we analyzed bone marrow adipose tissue (BMAT) as another potential mechanism regulating the observed skeletal phenotypes. We found an increase in bone marrow adipocyte size in the *Dnmt3a*$^{R878H/+}$ mutant mice that has not been associated with TBRS patients. Within bone marrow, *DNMT3A* has been studied extensively in the context of clonal hematopoiesis (CH) and acute myeloid leukemia (AML) where hematopoietic stem cells in bone marrow develop cancerous mutations. The *DNMT3A*$^{R882H/+}$ mutation found in TBRS patients is also the most prevalent mutation associated with AML [24,47], but spontaneous hematopoietic malignancies (including AML) have not been reported before 12 months of age in the *Dnmt3a*$^{R878H/+}$ mice used in this work [9]. This suggests that the changes in the bone observed here occur in advance of the impacts of AML. Studies suggest that hematopoietic bone marrow cells with the *DNMT3A*$^{R882H/+}$ mutation do not respond to inflammatory cytokines secreted by bone marrow adipocytes [48,49]. Bone marrow adiposity is another example of the *DNMT3A*$^{R882H/+}$ mutation causing a broader and more severe array of phenotypes compared to *DNMT3A*$^{P904L/+}$ and other mutations. This correlates with stronger methylation effects observed in peripheral blood cells from TBRS patients with the *DNMT3A*$^{R882H/+}$ mutation [9]. Given that osteoclasts originate from hematopoietic progenitors, future studies of intercellular communication between hematopoietic progenitors and bone marrow adipocytes may help identify molecular mechanisms responsible for skeletal abnormalities typical of mice with the *Dnmt3a*$^{R878H/+}$ mutation.

The presence of overgrowth, cortical thinning, and compromised mechanical properties in both the *Dnmt3a*$^{P900L/+}$ and the *Dnmt3a*$^{R878H/+}$ mutant animals suggests a common mechanism that is not driven by increased body weight alone. Developmentally, skeletal tissue is derived from the mesoderm (axial and appendicular skeleton) and neural crest (craniofacial skeleton) [50]. Developmental studies have shown that *Dnmt3a* expression is endogenously low in the mesoderm and much higher in the ectoderm at mouse embryonic day 7.5. However, Dnmt3a expression is ubiquitous by embryonic day 8.5 [5]. Mesoderm-derived bone marrow mesenchymal stromal cells give rise to chondrocytes, adipocytes, and osteoblasts [51] while the ectoderm gives rise to the epidermis, the central nervous system, and peripheral nervous system [52]. A previous study indicates that *Wnt3a*-induced *DNMT3A* expression methylates the *SOX9* promotor in human limb bud mesenchymal cells, but *FGF2* and *FGF8* can block *DNMT3A* methylation by activating ERK1/2 phosphorylation of *DNMT3A* [53]. This study examined several mutations in *DNMT3A* with modifications at the ERK1/2 docking site or phosphorylation site and found significant differences in *SOX9* methylation in the presence of those mutants. Future work should investigate what binding sites are modified by the *Dnmt3a*$^{R878H/+}$ and *Dnmt3a*$^{P900L/+}$ mutations to identify what molecular mechanisms may be impacted. The more consistent phenotypes (long bone overgrowth and cortical bone thinning) may be set into motion in the mesoderm during early embryonic development. Meanwhile, the mutation-specific changes,

such as bone marrow adipose tissue development and behavioral abnormalities [9,11], may compound during the later stages of gestation when the mutant *Dnmt3a* enzyme is more abundant. Future developmental studies will provide critical information for understanding the origins of skeletal abnormalities and neurodevelopmental disorders present in TBRS patients.

While this study has identified new skeletal phenotypes in specific *Dnmt3a* OGID mouse models, questions about cellular and molecular mechanism remain unanswered. In our study, we chose an early postnatal timepoint (P27) to study osteoblast, osteoclast, and growth plate activity. While there are differences in growth plate thickness, the cellular processes responsible for that overgrowth are unclear. Meanwhile, osteoblast activity and osteoclast size and number are unchanged at P27, leaving the cellular mechanism for cortical thinning unresolved. Future studies involving DNA methylation profiling and RNA-Seq transcriptomic analyses will be useful for determining the cells and molecular pathways that are impacted by mutations in *Dnmt3a*. Moreover, studies of Cre-inducible $Dnmt3a^{fl\text{-}R878H}$ mice (JAX Stock No. 032289) can be useful for differentiating developmental effects of the mutation from disruptions in homeostasis [54]. Additional studies investigating the in vivo differentiation timeline of mesenchymal and neural crest cells may provide critical insights into identifying a common mechanism for the skeletal and neurodevelopmental abnormalities present in OGID patients.

An additional shortcoming of the present study is the lack of direct comparison between mutant groups. Breeding animals to generate wild-type, $Dnmt3a^{P900L/+}$, and $Dnmt3a^{R878H/+}$ mice in the same litter will allow direct comparisons between strains, and can improve our understanding of the similarities and differences between the two mutations. While previous studies have characterized the effects of the $Dnmt3a^{R878H/+}$ and $Dnmt3a^{P900L/+}$ mutations on the methylome and transcriptome, those studies have been carried out in peripheral blood cells and neurons which are distinct from the cells involved in skeletal development. Future studies can address the shortcomings mentioned herein and further elucidate the mechanisms responsible for causing overgrowth in TBRS and other OGID-class disorders.

In conclusion, DNMT3A plays a critical role in skeletal development, impacting growth plate chondrocytes and bone marrow adipocytes. *Dnmt3a* point mutations $Dnmt3a^{R878H/+}$ and $Dnmt3a^{P900L/+}$, both of which are homologous to mutations found in human TBRS patients, dysregulate murine skeletal development in multiple ways, some of which are established phenotypes of TBRS patients. The findings reported in this study should be used as a groundwork for future studies in mouse models of TBRS and other OGID mouse models. Several of the reported findings have not yet been investigated in humans and assessment in the clinical population would be warranted. A better understanding of skeletal abnormalities in TBRS can potentially be useful in improving diagnosis, treatment, and quality of life for these patients.

Supplementary data to this article can be found online at https://doi.org/10.1016/j.bone.2024.117085.

Supplementary Material

Refer to Web version on PubMed Central for supplementary material.

Acknowledgments

The authors would like to thank the cores and staff of the Washington University Musculoskeletal Research Center for their assistance. Specifically, thanks to Crystal Idleburg and Samantha Coleman for histological processing and sectioning, Michael Brodt and Matthew Silva for assistance in biomechanical analyses, Nicole Migotsky and Matthew Silva for support in dynamic histomorphometry, and Xiao Zhang for facilitating bone marrow adipose tissue analyses.

Grants

This work was supported by the National Institutes of Health [grant numbers R01 MH117405 (to H.G.), R01 AR075730 (to A.M.), F31 HD100098 (to D.C.B.), F31 AR082294 (to A. B.)] and The Simons Foundation Autism Research Initiative, New York, NY. Support for histology, microCT and biomechanical assays was provided by the Washington University Musculoskeletal Research Center (NIH P30 AR074992 and S10 OD028573). Histology slides were imaged with the Nanozoomer at Alafi Neuroimaging Core (S10 RR027552). The content is solely the responsibility of the authors and does not necessarily represent the official views of the National Institutes of Health.

Data availability

Data will be made available on request.

References

[1]. Manor J, Lalani SR, Overgrowth syndromes-evaluation, diagnosis, and management, Front. Pediatr 8 (2020) 574857. [PubMed: 33194904]

[2]. Adam MP, Feldman J, Mirzaa GM, Pagon RA, Wallace SE, Bean LJH, Gripp KW, Amemiya A, GeneReviews, 1993.

[3]. Sabin MA, Werther GA, Kiess W, Genetics of obesity and overgrowth syndromes, Best Pract. Res. Clin. Endocrinol. Metab 25 (1) (2011) 207–220. [PubMed: 21396586]

[4]. Tatton-Brown K, Loveday C, Yost S, Clarke M, Ramsay E, Zachariou A, Elliott A, Wylie H, Ardissone A, Rittinger O, Stewart F, Temple IK, Cole T, Mahamdallie S, Seal S, Ruark E, Rahman N, Collaboration CO, Mutations in epigenetic regulation genes are a major cause of overgrowth with intellectual disability, Am. J. Hum. Genet 100 (5) (2017) 725–736. [PubMed: 28475857]

[5]. Okano M, Bell DW, Haber DA, Li E, DNA methyltransferases Dnmt3a and Dnmt3b are essential for de novo methylation and mammalian development, Cell 99 (3) (1999) 247–257. [PubMed: 10555141]

[6]. Ostrowski PJ, Tatton-Brown K, Tatton-Brown-Rahman syndrome, in: Adam MP, Mirzaa GM, Pagon RA, Wallace SE, Bean LJH, Gripp KW, Amemiya A (Eds.), GeneReviews(®), © 1993–2023, University of Washington, Seattle, GeneReviews is a registered trademark of the University of Washington, Seattle, Seattle WA, 1993.

[7]. Tatton-Brown K, Seal S, Ruark E, Harmer J, Ramsay E, Del Vecchio Duarte S, Zachariou A, Hanks S, O'Brien E, Aksglaede L, Baralle D, Dabir T, Gener B, Goudie D, Homfray T, Kumar A, Pilz DT, Selicorni A, Temple IK, Van Maldergem L, Yachelevich N, van Montfort R, Rahman N, Consortium CO, Mutations in the DNA methyltransferase gene DNMT3A cause an overgrowth syndrome with intellectual disability, Nat. Genet 46 (4) (2014) 385–388. [PubMed: 24614070]

[8]. Tatton-Brown K, Zachariou A, Loveday C, Renwick A, Mahamdallie S, Aksglaede L, Baralle D, Barge-Schaapveld D, Blyth M, Bouma M, Breckpot J, Crabb B, Dabir T, Cormier-Daire V, Fauth C, Fisher R, Gener B, Goudie D, Homfray T, Hunter M, Jorgensen A, Kant SG, Kirally-Borri C, Koolen D, Kumar A, Labilloy A, Lees M, Marcelis C, Mercer C, Mignot C, Miller K, Neas

K, Newbury-Ecob R, Pilz DT, Posmyk R, Prada C, Ramsey K, Randolph LM, Selicorni A, Shears D, Suri M, Temple IK, Turnpenny P, Val Maldergem L, Varghese V, Veenstra-Knol HE, Yachelevich N, Yates L, Rahman N, C.A.o.t.U.o.S.a.E.a.a.S.C.R. Study, D.D.D.D. Study, The Tatton-Brown-Rahman Syndrome: a clinical study of 55 individuals with, Wellcome Open Res 3 (2018) 46. [PubMed: 29900417]

[9]. Smith AM, LaValle TA, Shinawi M, Ramakrishnan SM, Abel HJ, Hill CA, Kirkland NM, Rettig MP, Helton NM, Heath SE, Ferraro F, Chen DY, Adak S, Semenkovich CF, Christian DL, Martin JR, Gabel HW, Miller CA, Ley TJ, Functional and epigenetic phenotypes of humans and mice with DNMT3A Overgrowth Syndrome, Nat. Commun 12 (1) (2021) 4549. [PubMed: 34315901]

[10]. Christian DL, Wu DY, Martin JR, Moore JR, Liu YR, Clemens AW, Nettles SA, Kirkland NM, Papouin T, Hill CA, Wozniak DF, Dougherty JD, Gabel HW, DNMT3A haploinsufficiency results in behavioral deficits and global epigenomic dysregulation shared across neurodevelopmental disorders, Cell Rep 33 (8) (2020) 108416. [PubMed: 33238114]

[11]. Beard DC, Zhang X, Wu DY, Martin JR, Erickson A, Boua JV, Hamagami N, Swift RG, McCullough KB, Ge X, Bell-Hensley A, Zheng H, Palmer CW, Fuhler NA, Lawrence AB, Hill CA, Papouin T, Noguchi KK, McAlinden A, Garbow JR, Dougherty JD, Maloney SE, Gabel HW, Distinct disease mutations in DNMT3A result in a spectrum of behavioral, epigenetic, and transcriptional deficits, Cell Rep 42 (11) (2023) 113411. [PubMed: 37952155]

[12]. Cohen MM, The large-for-gestational-age (LGA) infant in dysmorphic perspective, in: Willey AM, Carter TP, Kelly S, Porter IH (Eds.), Clinical Genetics, Academic Press, 1982, pp. 153–169.

[13]. Tatton-Brown K, Weksberg R, Molecular mechanisms of childhood overgrowth, Am. J. Med. Genet. C: Semin. Med. Genet 163C (2) (2013) 71–75. [PubMed: 23606607]

[14]. Cytrynbaum CS, Smith AC, Rubin T, Weksberg R, Advances in overgrowth syndromes: clinical classification to molecular delineation in Sotos syndrome and Beckwith-Wiedemann syndrome, Curr. Opin. Pediatr 17 (6) (2005) 740–746. [PubMed: 16282780]

[15]. Nixon JP, Zhang M, Wang C, Kuskowski MA, Novak CM, Levine JA, Billington CJ, Kotz CM, Evaluation of a quantitative magnetic resonance imaging system for whole body composition analysis in rodents, Obesity (Silver Spring) 18 (8) (2010) 1652–1659. [PubMed: 20057373]

[16]. Bouxsein ML, Boyd SK, Christiansen BA, Guldberg RE, Jepsen KJ, Müller R, Guidelines for assessment of bone microstructure in rodents using micro-computed tomography, J. Bone Miner. Res 25 (7) (2010) 1468–1486. [PubMed: 20533309]

[17]. Jepsen KJ, Silva MJ, Vashishth D, Guo XE, van der Meulen MC, Establishing biomechanical mechanisms in mouse models: practical guidelines for systematically evaluating phenotypic changes in the diaphyses of long bones, J. Bone Miner. Res 30 (6) (2015) 951–966. [PubMed: 25917136]

[18]. Scheller EL, Troiano N, Vanhoutan JN, Bouxsein MA, Fretz JA, Xi Y, Nelson T, Katz G, Berry R, Church CD, Doucette CR, Rodeheffer MS, Macdougald OA, Rosen CJ, Horowitz MC, Use of osmium tetroxide staining with microcomputerized tomography to visualize and quantify bone marrow adipose tissue in vivo, Methods Enzymol 537 (2014) 123–139. [PubMed: 24480344]

[19]. Scheller EL, Doucette CR, Learman BS, Cawthorn WP, Khandaker S, Schell B, Wu B, Ding SY, Bredella MA, Fazeli PK, Khoury B, Jepsen KJ, Pilch PF, Klibanski A, Rosen CJ, MacDougald OA, Region-specific variation in the properties of skeletal adipocytes reveals regulated and constitutive marrow adipose tissues, Nat. Commun 6 (2015) 7808. [PubMed: 26245716]

[20]. Dempster DW, Compston JE, Drezner MK, Glorieux FH, Kanis JA, Malluche H, Meunier PJ, Ott SM, Recker RR, Parfitt AM, Standardized nomenclature, symbols, and units for bone histomorphometry: a 2012 update of the report of the ASBMR Histomorphometry Nomenclature Committee, J. Bone Miner. Res 28 (1) (2013) 2–17. [PubMed: 23197339]

[21]. Lawson LY, Brodt MD, Migotsky N, Chermside-Scabbo CJ, Palaniappan R, Silva MJ, Osteoblast-specific Wnt secretion is required for skeletal homeostasis and loading-induced bone formation in adult mice, J. Bone Miner. Res 37 (1) (2022) 108–120. [PubMed: 34542191]

[22]. Erben RG, Embedding of bone samples in methylmethacrylate: an improved method suitable for bone histomorphometry, histochemistry, and immunohistochemistry, J. Histochem. Cytochem 45 (2) (1997) 307–313. [PubMed: 9016319]

[23]. Glatt V, Canalis E, Stadmeyer L, Bouxsein ML, Age-related changes in trabecular architecture differ in female and male C57BL/6J mice, J. Bone Miner. Res 22 (8) (2007) 1197–1207. [PubMed: 17488199]

[24]. Ley TJ, Ding L, Walter MJ, McLellan MD, Lamprecht T, Larson DE, Kandoth C, Payton JE, Baty J, Welch J, Harris CC, Lichti CF, Townsend RR, Fulton RS, Dooling DJ, Koboldt DC, Schmidt H, Zhang Q, Osborne JR, Lin L, O'Laughlin M, McMichael JF, Delehaunty KD, McGrath SD, Fulton LA, Magrini VJ, Vickery TL, Hundal J, Cook LL, Conyers JJ, Swift GW, Reed JP, Alldredge PA, Wylie T, Walker J, Kalicki J, Watson MA, Heath S, Shannon WD, Varghese N, Nagarajan R, Westervelt P, Tomasson MH, Link DC, Graubert TA, DiPersio JF, Mardis ER, Wilson RK, DNMT3A mutations in acute myeloid leukemia, N. Engl. J. Med 363 (25) (2010) 2424–2433. [PubMed: 21067377]

[25]. Ferguson VL, Ayers RA, Bateman TA, Simske SJ, Bone development and age-related bone loss in male C57BL/6J mice, Bone 33 (3) (2003) 387–398. [PubMed: 13678781]

[26]. Brodt MD, Ellis CB, Silva MJ, Growing C57Bl/6 mice increase whole bone mechanical properties by increasing geometric and material properties, J. Bone Miner. Res 14 (12) (1999) 2159–2166. [PubMed: 10620076]

[27]. Wilson K, Usami Y, Hogarth D, Scheiber AL, Tian H, Oichi T, Wei Y, Qin L, Otsuru S, Toyosawa S, Iwamoto M, Abzug JM, Enomoto-Iwamoto M, Analysis of association between morphometric parameters of growth plate and bone growth of tibia in mice and humans, Cartilage 13 (2_suppl) (2021) 315S–325S. [PubMed: 31997656]

[28]. Foldes J, Shih MS, Parfitt AM, Frequency distributions of tetracycline-based measurements: implications for the interpretation of bone formation indices in the absence of double-labeled surfaces, J. Bone Miner. Res 5 (10) (1990) 1063–1067. [PubMed: 2080717]

[29]. Nguyen S, Meletis K, Fu D, Jhaveri S, Jaenisch R, Ablation of de novo DNA methyltransferase Dnmt3a in the nervous system leads to neuromuscular defects and shortened lifespan, Dev. Dyn 236 (6) (2007) 1663–1676. [PubMed: 17477386]

[30]. Tovy A, Reyes JM, Zhang L, Huang YH, Rosas C, Daquinag AC, Guzman A, Ramabadran R, Chen CW, Gu T, Gupta S, Ortinau L, Park D, Cox AR, Rau RE, Hartig SM, Kolonin MG, Goodell MA, Constitutive loss of DNMT3A causes morbid obesity through misregulation of adipogenesis, Elife 11 (2022).

[31]. Eswarakumar VP, Schlessinger J, Skeletal overgrowth is mediated by deficiency in a specific isoform of fibroblast growth factor receptor 3, Proc. Natl. Acad. Sci. U. S. A 104 (10) (2007) 3937–3942. [PubMed: 17360456]

[32]. Kondo E, Yasoda A, Tsuji T, Fujii T, Miura M, Kanamoto N, Tamura N, Arai H, Kunieda T, Nakao K, Skeletal analysis of the long bone abnormality (lbab/lbab) mouse, a novel chondrodysplastic C-type natriuretic peptide mutant, Calcif. Tissue Int 90 (4) (2012) 307–318. [PubMed: 22271248]

[33]. Miao D, Liu H, Plut P, Niu M, Huo R, Goltzman D, Henderson JE, Impaired endochondral bone development and osteopenia in Gli2-deficient mice, Exp. Cell Res 294 (1) (2004) 210–222. [PubMed: 14980515]

[34]. Nishikawa K, Iwamoto Y, Kobayashi Y, Katsuoka F, Kawaguchi S, Tsujita T, Nakamura T, Kato S, Yamamoto M, Takayanagi H, Ishii M, DNA methyltransferase 3a regulates osteoclast differentiation by coupling to an S-adenosylmethionine-producing metabolic pathway, Nat. Med 21 (3) (2015) 281–287. [PubMed: 25706873]

[35]. Liu H, Liu Z, Du J, He J, Lin P, Amini B, Starbuck MW, Novane N, Shah JJ, Davis RE, Hou J, Gagel RF, Yang J, Thymidine phosphorylase exerts complex effects on bone resorption and formation in myeloma, Sci. Transl. Med 8 (353) (2016) 353ra113.

[36]. Tice MJL, Bailey S, Sroga GE, Gallagher EJ, Vashishth D, Non-obese MKR mouse model of type 2 diabetes reveals skeletal alterations in mineralization and material properties, JBMR Plus 6 (2) (2022) e10583. [PubMed: 35229063]

[37]. Kawashima Y, Fritton JC, Yakar S, Epstein S, Schaffler MB, Jepsen KJ, LeRoith D, Type 2 diabetic mice demonstrate slender long bones with increased fragility secondary to increased osteoclastogenesis, Bone 44 (4) (2009) 648–655. [PubMed: 19150422]

[38]. Morris MD, Mandair GS, Raman assessment of bone quality, Clin. Orthop. Relat. Res 469 (8) (2011) 2160–2169. [PubMed: 21116756]

[39]. Lewis G, Nyman JS, The use of nanoindentation for characterizing the properties of mineralized hard tissues: state-of-the art review, J Biomed Mater Res B Appl Biomater 87 (1) (2008) 286–301. [PubMed: 18395829]

[40]. Mabilleau G, Perrot R, Flatt PR, Irwin N, Chappard D, High fat-fed diabetic mice present with profound alterations of the osteocyte network, Bone 90 (2016) 99–106. [PubMed: 27312542]

[41]. Ma C, Du T, Niu X, Fan Y, Biomechanics and mechanobiology of the bone matrix, Bone Res 10 (1) (2022) 59. [PubMed: 36042209]

[42]. Silva MJ, Brodt MD, Wopenka B, Thomopoulos S, Williams D, Wassen MH, Ko M, Kusano N, Bank RA, Decreased collagen organization and content are associated with reduced strength of demineralized and intact bone in the SAMP6 mouse, J. Bone Miner. Res 21 (1) (2006) 78–88. [PubMed: 16355276]

[43]. Tang SY, Herber RP, Ho SP, Alliston T, Matrix metalloproteinase-13 is required for osteocytic perilacunar remodeling and maintains bone fracture resistance, J. Bone Miner. Res 27 (9) (2012) 1936–1950. [PubMed: 22549931]

[44]. Collins KH, Lenz KL, Pollitt EN, Ferguson D, Hutson I, Springer LE, Oestreich AK, Tang R, Choi YR, Meyer GA, Teitelbaum SL, Pham CTN, Harris CA, Guilak F, Adipose tissue is a critical regulator of osteoarthritis, Proc. Natl. Acad. Sci. U. S. A 118 (1) (2021).

[45]. Hawkes CP, Mostoufi-Moab S, Fat-bone interaction within the bone marrow milieu: impact on hematopoiesis and systemic energy metabolism, Bone 119 (2019) 57–64. [PubMed: 29550266]

[46]. Scheller EL, Rosen CJ, What's the matter with MAT? Marrow adipose tissue, metabolism, and skeletal health, Ann. N. Y. Acad. Sci 1311 (1) (2014) 14–30. [PubMed: 24650218]

[47]. Jaiswal S, Fontanillas P, Flannick J, Manning A, Grauman PV, Mar BG, Lindsley RC, Mermel CH, Burtt N, Chavez A, Higgins JM, Moltchanov V, Kuo FC, Kluk MJ, Henderson B, Kinnunen L, Koistinen HA, Ladenvall C, Getz G, Correa A, Banahan BF, Gabriel S, Kathiresan S, Stringham HM, McCarthy MI, Boehnke M, Tuomilehto J, Haiman C, Groop L, Atzmon G, Wilson JG, Neuberg D, Altshuler D, Ebert BL, Age-related clonal hematopoiesis associated with adverse outcomes, N. Engl. J. Med 371 (26) (2014) 2488–2498. [PubMed: 25426837]

[48]. Liao M, Chen R, Yang Y, He H, Xu L, Jiang Y, Guo Z, He W, Jiang H, Wang J, Aging-elevated inflammation promotes DNMT3A R878H-driven clonal hematopoiesis, Acta Pharm. Sin. B 12 (2) (2022) 678–691. [PubMed: 35256939]

[49]. Zioni N, Bercovich AA, Chapal-Ilani N, Bacharach T, Rappoport N, Solomon A, Avraham R, Kopitman E, Porat Z, Sacma M, Hartmut G, Scheller M, Muller-Tidow C, Lipka D, Shlush E, Minden M, Kaushansky N, Shlush LI, Inflammatory signals from fatty bone marrow support DNMT3A driven clonal hematopoiesis, Nat. Commun 14 (1) (2023) 2070. [PubMed: 37045808]

[50]. Nakashima K, de Crombrugghe B, Transcriptional mechanisms in osteoblast differentiation and bone formation, Trends Genet 19 (8) (2003) 458–466. [PubMed: 12902164]

[51]. Gao Q, Wang L, Wang S, Huang B, Jing Y, Su J, Bone marrow mesenchymal stromal cells: identification, classification, and differentiation, Front. Cell Dev. Biol 9 (2021) 787118. [PubMed: 35047499]

[52]. Sasai Y, De Robertis EM, Ectodermal patterning in vertebrate embryos, Dev. Biol 182 (1) (1997) 5–20. [PubMed: 9073437]

[53]. Kumar D, Lassar AB, Fibroblast growth factor maintains chondrogenic potential of limb bud mesenchymal cells by modulating DNMT3A recruitment, Cell Rep 8 (5) (2014) 1419–1431. [PubMed: 25159139]

[54]. Loberg MA, Bell RK, Goodwin LO, Eudy E, Miles LA, SanMiguel JM, Young K, Bergstrom DE, Levine RL, Schneider RK, Trowbridge JJ, Sequentially inducible mouse models reveal that Npm1 mutation causes malignant transformation of Dnmt3a-mutant clonal hematopoiesis, Leukemia 33 (7) (2019) 1635–1649. [PubMed: 30692594]

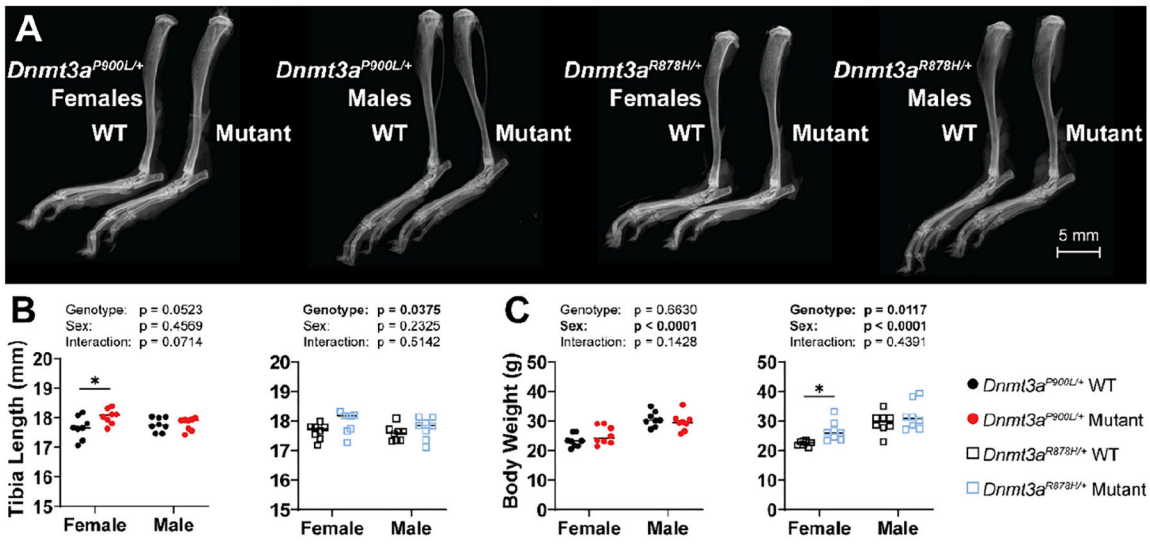

Fig. 1.

Analysis of tibia length and body weight in *Dnmt3a*$^{P900L/+}$ and *Dnmt3a*$^{R878H/+}$ mice. A) Representative X-ray images of tibias from wild-type (WT) and mutant (*Dnmt3a*$^{P900L/+}$ or *Dnmt3a*$^{R878H/+}$) mice. B) Graphical representation of tibia lengths for WT and mutant littermates. C) Graphical representation of body weights in WT and mutant mice. Symbols indicate significance in post hoc testing: * $p < 0.05$. $n = 8$/mutation/sex/strain. ANOVA terms are displayed above the graphs, bolded terms have $p < 0.05$. For full ANOVA analysis, see Supplementary Table 1.

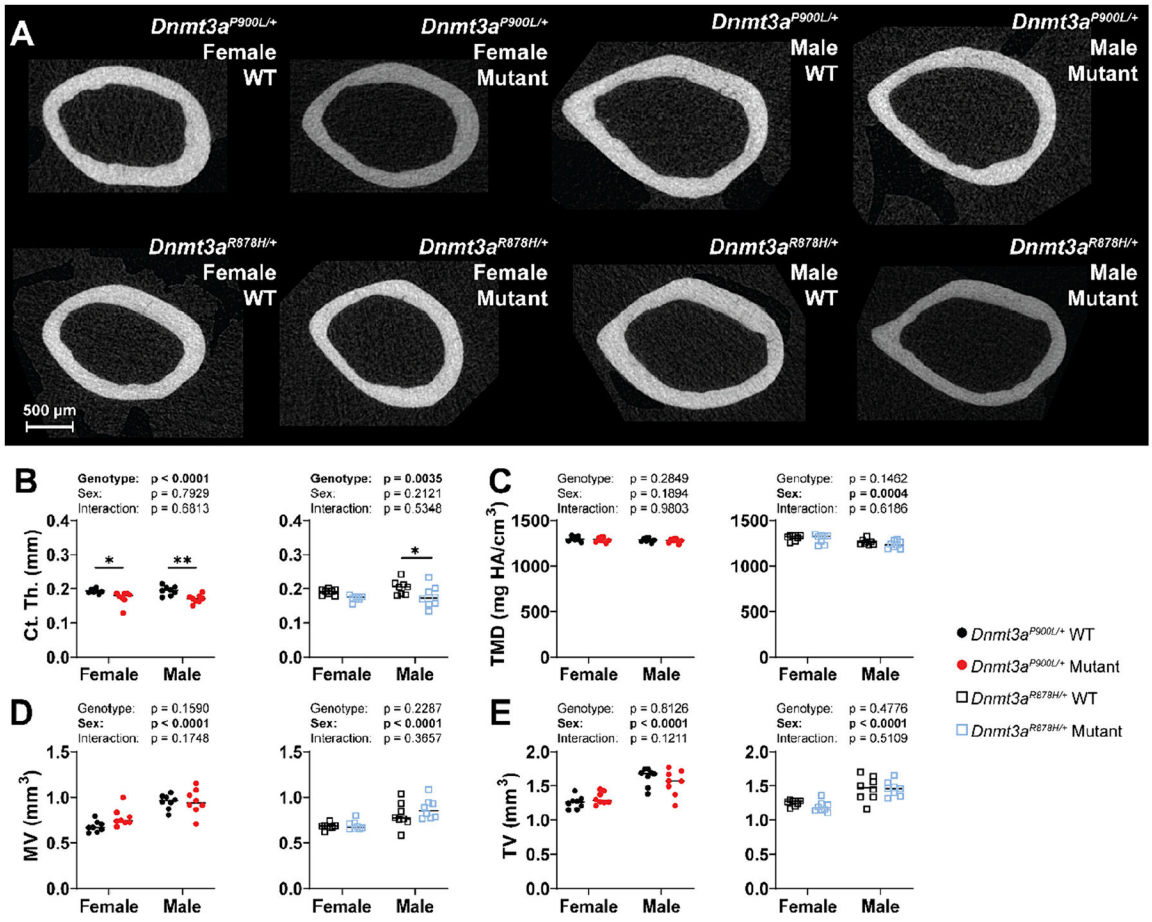

Fig. 2.

Analysis of femoral cortical bone thickness and mineral density in *Dnmt3a*$^{P900L/+}$ and *Dnmt3a*$^{R878H/+}$ mice. (A) Representative images of cortical bone from femurs of wild-type (WT) and mutant (*Dnmt3a*$^{P900L/+}$ or *Dnmt3a*$^{R878H/+}$) mice. B-E) Graphical representation of µCT B) cortical thickness, C) cortical tissue mineral density, D) marrow volume, and E) total volume data. Symbols indicate significance in post hoc testing: * $p < 0.05$, ** $p < 0.01$. $n = 8$/mutation/sex/strain. ANOVA terms are displayed above the graphs, bolded terms have $p < 0.05$. For full ANOVA analysis, see Supplementary Table 1.

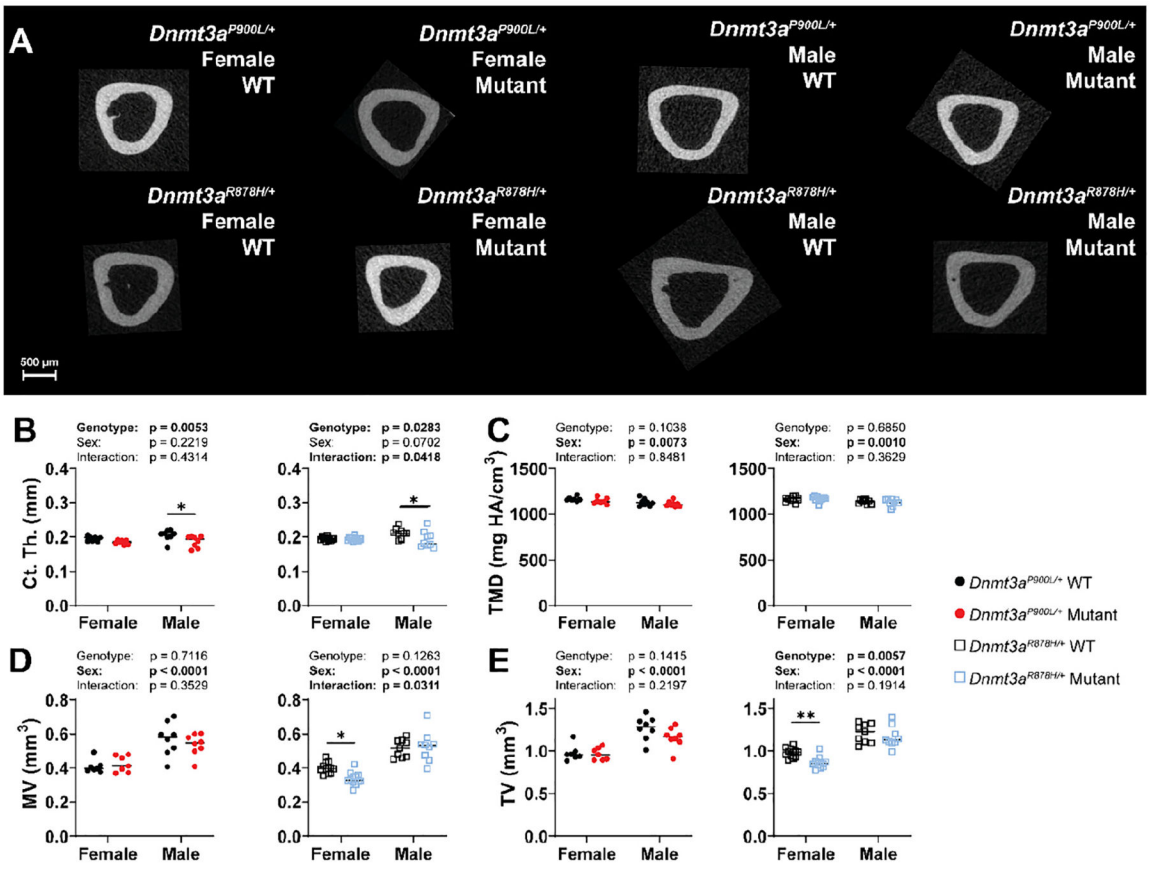

Fig. 3.

Analysis of tibial cortical bone thickness and mineral density in *Dnmt3a*$^{P900L/+}$ and *Dnmt3a*$^{R878H/+}$ mice. (A) Representative images of cortical bone from tibias of wild-type (WT) and mutant (*Dnmt3a*$^{P900L/+}$ or *Dnmt3a*$^{R878H/+}$) mice. B-E) Graphical representation of µCT B) cortical thickness, C) cortical tissue mineral density, D) marrow volume, and E) total volume data. Symbols indicate significance in post hoc testing: * $p < 0.05$. n = 7–12/mutation/sex/strain. ANOVA terms are displayed above the graphs, bolded terms have $p < 0.05$. For full ANOVA analysis, see Supplementary Table 1.

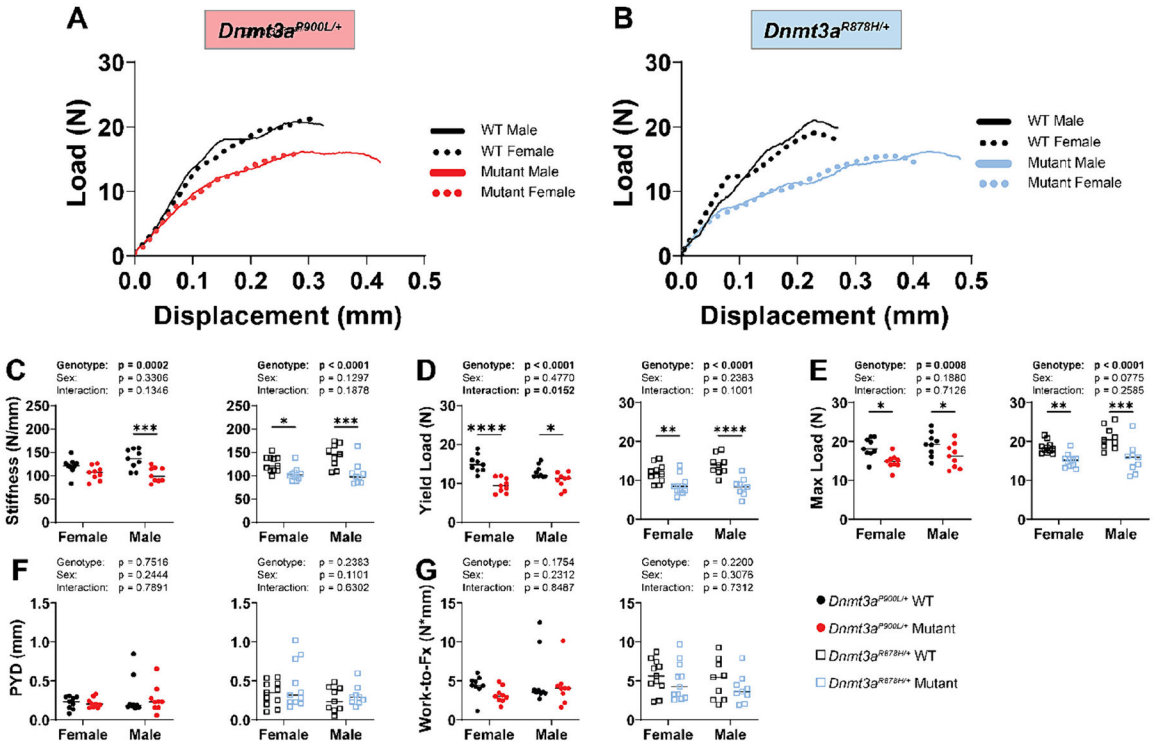

Fig. 4.

Three-point bend testing data of femurs from *Dnmt3a*$^{P900L/+}$ and *Dnmt3a*$^{R878H/+}$ mice. A-B) Representative load-displacement curves from three-point bend testing of A) *Dnmt3a*$^{P900L/+}$ and B) *Dnmt3a*$^{R878H/+}$ littermate pairs aged 30–36 weeks. C-G) Graphical representation of C) stiffness, D) yield load, E) maximum load, F) post-yield displacement, and G) work-to-fracture data. Symbols indicate significance in post hoc testing: * $p < 0.05$, ** $p < 0.01$, *** $p < 0.001$, **** $p < 0.0001$. $n = 9–11$/mutation/sex/strain. ANOVA terms are displayed above the graphs, bolded terms have $p < 0.05$. For full ANOVA analysis, see Supplementary Table 1.

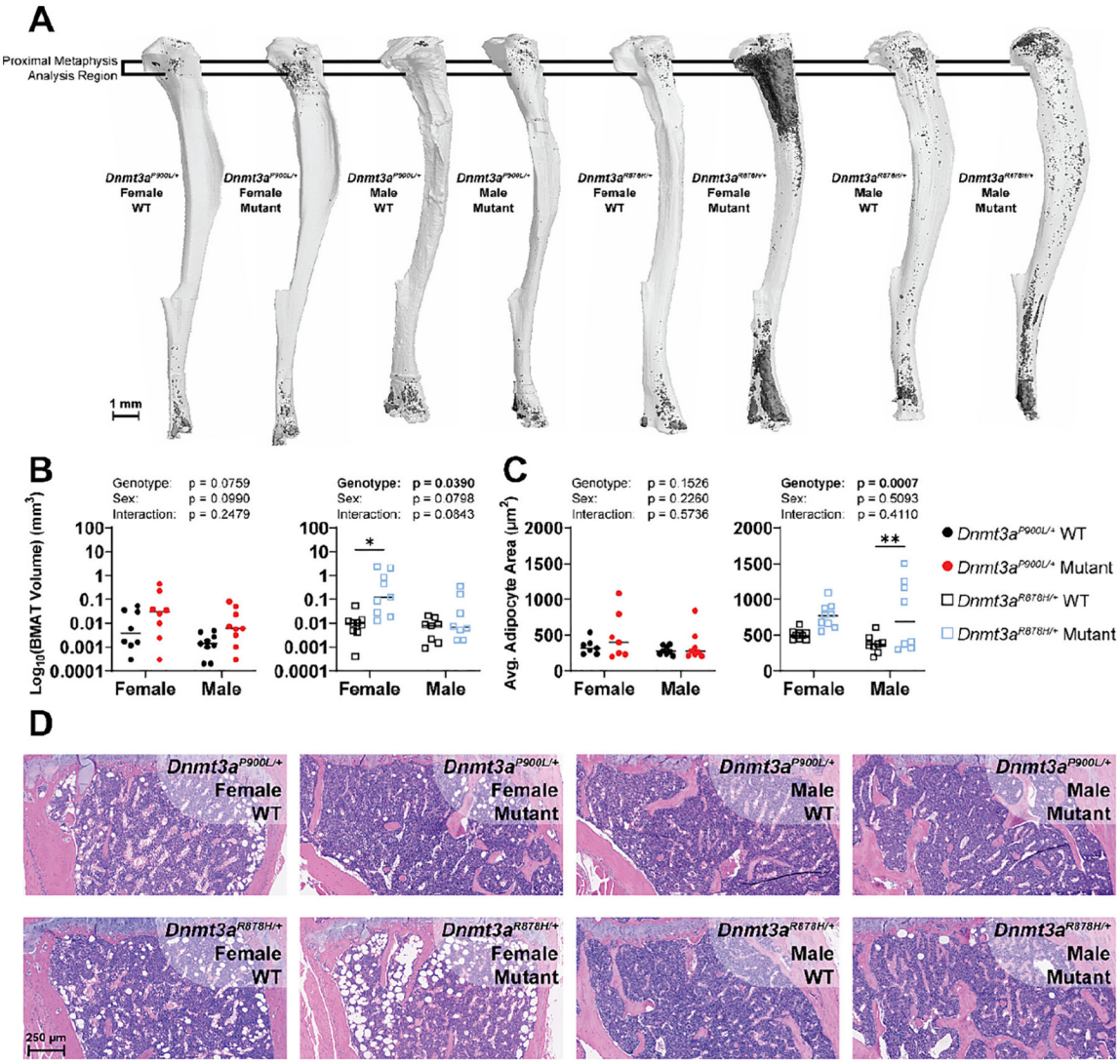

Fig. 5.

Analysis of bone marrow adipose tissue in *Dnmt3a*$^{P900L/+}$ and *Dnmt3a*$^{R878H/+}$ mice. A) Representative 3D reconstructions from µCT scans of osmium-stained tibias from littermate pairs of male and female mice from of wild-type (WT) and mutant (*Dnmt3a*$^{P900L/+}$ or *Dnmt3a*$^{R878H/+}$) genotypes. B) Osmium quantification in the proximal metaphysis of tibias from mature mice using a logarithmic scale (base 10). C) Average cross-sectional area of bone marrow adipocytes in H&E images. D) Representative H&E images of the proximal tibial metaphyses from WT and mutant mice. Symbols indicate significance in post hoc testing: * $p < 0.05$, ** $p < 0.01$. n = 7–9/mutation/sex/strain. ANOVA terms are displayed above the graphs, bolded terms have $p < 0.05$. For full ANOVA analysis, see Supplementary Table 1.

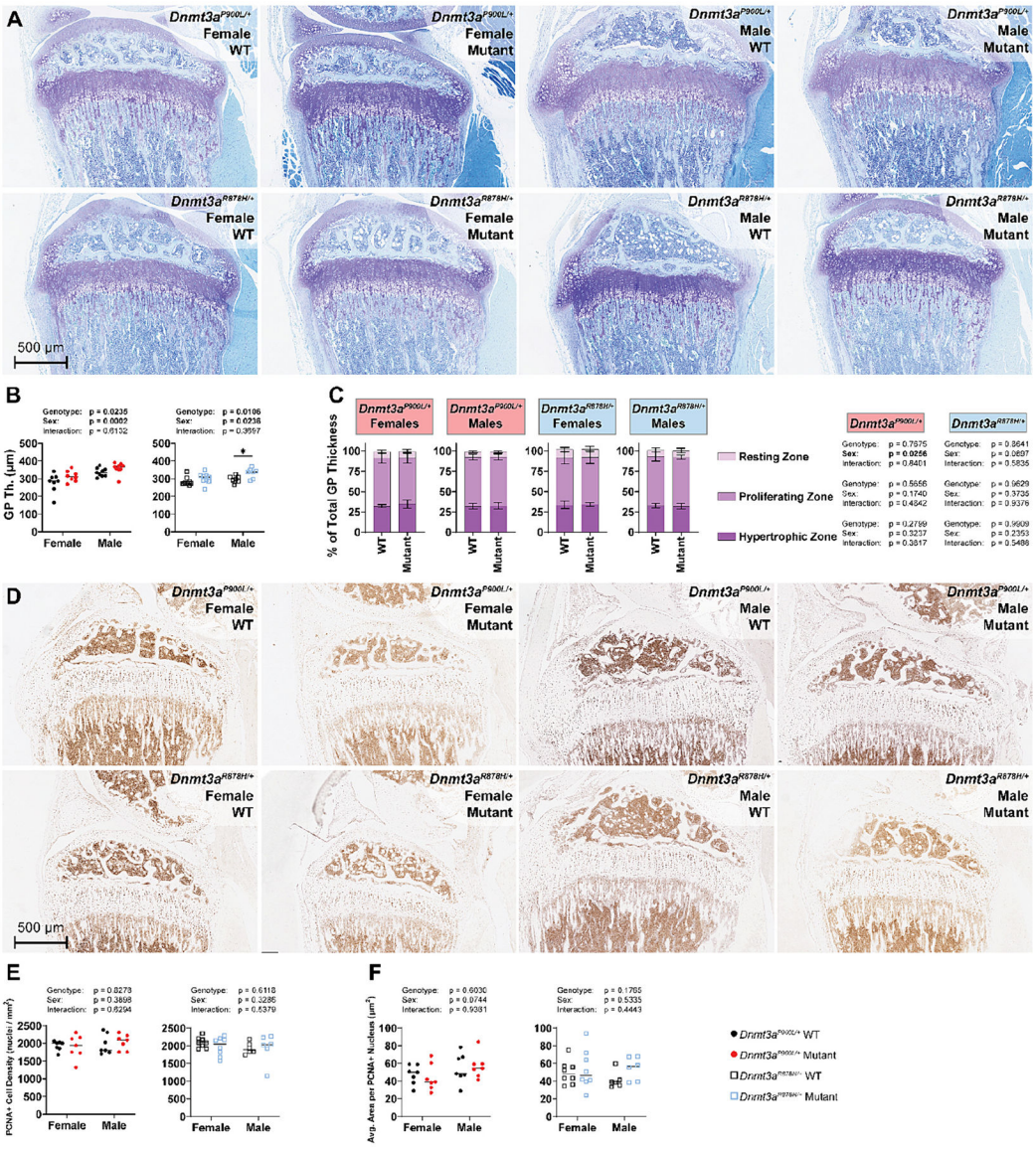

Fig. 6.

Analysis of thickness and proliferative activity in the proximal tibia growth plate in *Dnmt3a*$^{P900L/+}$ and *Dnmt3a*$^{R878H/+}$ mice. A) Representative toluidine blue images from the proximal growth plate of tibias from wild-type (WT) and mutant (*Dnmt3a*$^{P900L/+}$ or *Dnmt3a*$^{R878H/+}$) mice. B) Total growth plate thickness. C) Zonal proportions for the Resting Zone, Proliferating Zone, and Hypertrophic Zone in female and male mice. D) Representative PCNA IHC images from the proximal tibia growth plates of WT and mutant mice. E) Quantification of PCNA^{+} cell density. F) Quantification of PCNA^{+} cell cross-sectional area. Symbols indicate significance in post hoc testing: * $p < 0.05$. n = 6–9/mutation/sex/strain. Two-way ANOVA terms are displayed above the graphs and three-way ANOVA terms are displayed beside graph legends, bolded terms have p < 0.05. For full ANOVA analysis, see Supplementary Table 1.

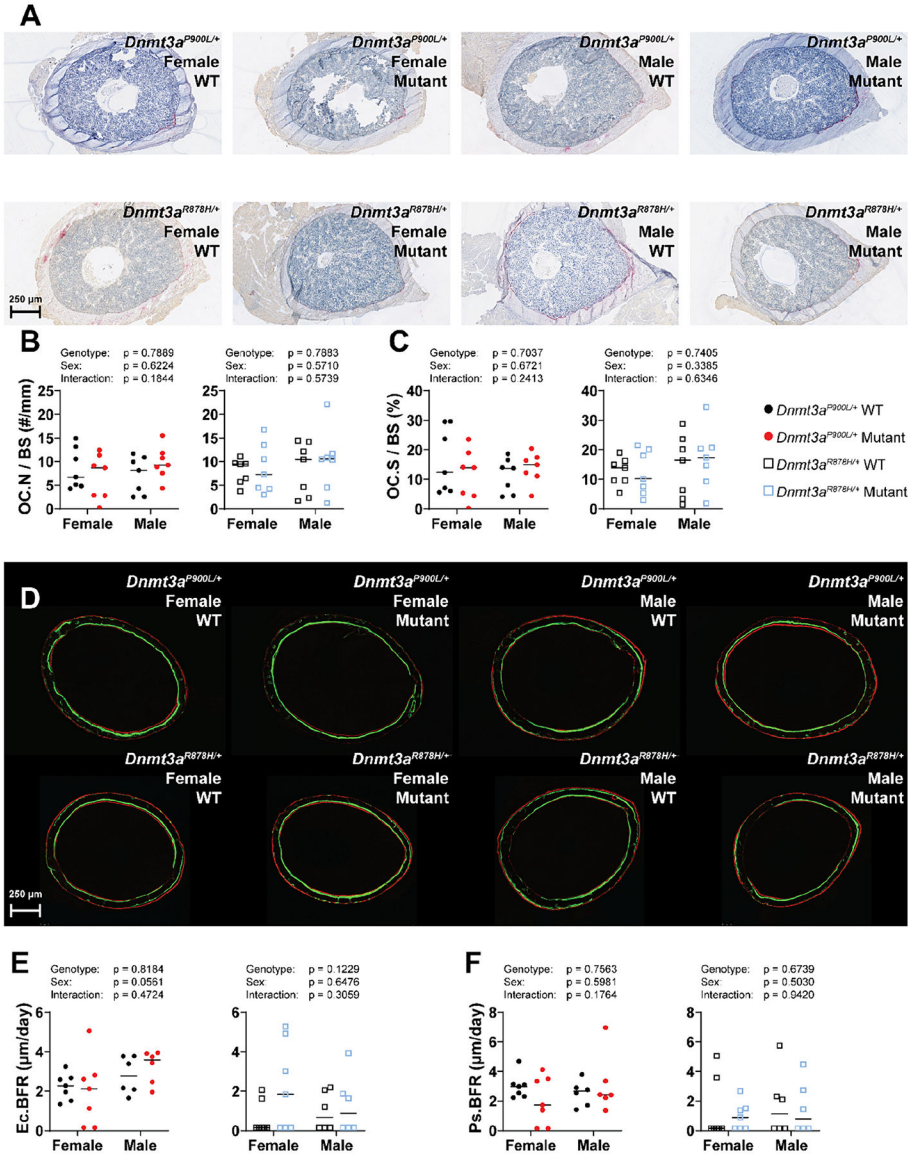

Fig. 7.

Bone formation and osteoclast number are unchanged by Dnmt3a mutations. A) Representative TRAP images from the femur mid-diaphysis of wild-type (WT) and mutant (*Dnmt3a*$^{P900L/+}$ or *Dnmt3a*$^{R878H/+}$) mice. B-C) Graphical representation of B) osteoclast number per bone surface (Oc.N/BS) and C) osteoclast surface per bone surface (Oc.S/BS). D) Representative dynamic histomorphometry images from the femur mid-diaphysis of wild-type (WT) and mutant (*Dnmt3a*$^{P900L/+}$ or *Dnmt3a*$^{R878H/+}$) mice.E-F) Graphical representation of E) endocortical bone formation rate (Ec.BFR) and F) periosteal bone formation rate (Ps.BFR). For BFR readouts, samples with no double labeled surface are set to 0.15 µm/day. n = 5–7/mutation/sex/strain. ANOVA terms are displayed above the graphs, bolded terms have $p < 0.05$. For full ANOVA analysis, see Supplementary Table 1.